PAPER

Check for updates

Multiphoton imaging and Raman spectroscopy of the bovine vertebral endplate†

Fay Crawford-Manning, [ID] ‡[a,b] Martha Z. Vardaki, [ID] *‡§[a,c] Ellen Green,[a] Judith R. Meakin, [ID] [a] Claudio Vergari, [ID] [a,d] Nick Stone [ID] [a] and C. Peter Winlove[a]

The interface between the intervertebral disc and the vertebral body is important to the discs' biomechanics and physiology, and is widely implicated in its pathology. This study aimed to explore biochemically and structurally the bony endplate, cartilage endplate and intervertebral disc, below the nucleus and below the annulus in healthy bovine tails. Multiphoton imaging and spontaneous Raman spectroscopy were employed. Raman spectroscopy provided relative quantification of mineral and matrix components across the vertebral endplate and its adjacent areas with microscopic spatial resolution. Microscopy utilising second-harmonic generation (SHG) and two-photon fluorescence (TPF) allowed for the structural identification of distinct endplate regions. The cartilage endplate was revealed as structurally distinct from both the bone and disc, supporting its biomechanical function as a transition zone between the soft and hard tissue components. The collagen fibres were continuous across the tidemark which defines the interface between the mineralised and non-mineralised regions of the endplate. Raman spectroscopy revealed gradients in phosphate and carbonate content through the depth of the endplate and also differences beneath the nucleus and annulus consistent with a higher rate of remodelling under the annulus.

Introduction

It is widely accepted that the cartilaginous endplate is a mechanical interface between the soft tissues of the intervertebral disc (IVD) and the vertebral bone (Fig. 1) and acts as a conduit to the movement of water, nutrients and metabolites between the two structures. However, there has been little detailed investigation of either function. For example, there have been several reports on the distribution of blood vessels in the interface region, but very few studies on water and solute transport through the matrix of the endplate itself and mechanical studies have largely concentrated on its role in disc rupture, demonstrating failure at the boundary between calcified and uncalcified tissue. However, a detailed analysis linking the structure and composition of the endplate region is still lacking, although it could inform hypotheses that degeneration of the endplate may be a factor in disc degeneration, with its wide spread clinical sequelae.[1]

There is some inconsistency in the literature even in the definition of the 'endplate'. Clinically, Modic changes, which are defined as the alterations in magnetic resonance imaging (MRI) signal intensity of the bone adjacent to a degenerated disc, are often described as endplate changes. However, Modic changes can affect up to 75% of the vertebral body, whereas

[a]*School of Physics and Astronomy, University of Exeter, Exeter, UK.*
E-mail: m.vardaki@uoi.gr
[b]*School of Primary, Community and Social Care, Keele University & Haywood Academic Rheumatology Centre, Stoke-on-Trent, UK*
[c]*Department of Medical Physics, School of Health Sciences, University of Ioannina, Ioannina, 45110, Greece*
[d]*Arts et Metiers Institute of Technology, Université Sorbonne Paris Nord, IBHGC – Institut de Biomécanique Humaine Georges Charpak, HESAM Université, F-75013 Paris, France*
†Electronic supplementary information (ESI) available. See DOI: 10.1039/d1an00702e
‡Equal contribution.
§Present address: Department of Medical Physics, School of Health Sciences, University of Ioannina, Ioannina, 45110, Greece.
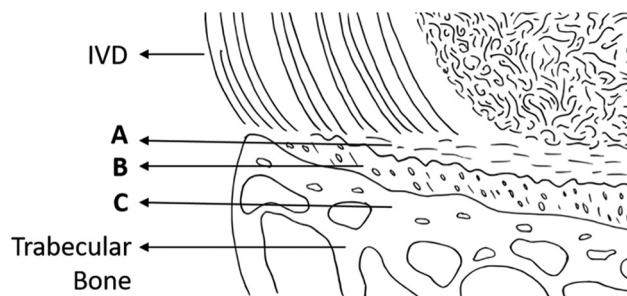
Fig. 1 Illustration of the transition from trabecular bone to the intervertebral disc (IVD), with the three regions of the vertebral endplate (A, B and C). (A) Non-mineralised cartilage (non-MC), (B) Mineralised Cartilage (MC), (C) Bony Endplate.

the endplate is believed to be as little as 1 mm in thickness.[2,3] In part, this confusion arises from attempting to be specific to the research questions, differing animal models[4] as well as limitations in the methodologies employed to investigate the tissue methods such as micro-CT have been used to visualise the mineralised tissue and MRI for the soft tissue. Further, imaging methods such as transmitted light (differential interface contrast or phase contrast) or electron (scanning (SEM) or transmission (TEM)) microscopy, require complex sample preparation including fixing and dehydrating, metal surface coating and the production of thin sections. Not only can thin sections limit the imaging for 3D structures in the tissue, but the preparation can produce artifacts when imaged. In this study, two novel and complementary techniques, multiphoton microscopy and Raman spectroscopy are used.

Second harmonic generation (SHG) is a multiphoton microscopic imaging technique that allows visualisation of fibrous collagen. It does not require specific sample preparation nor staining and, given the relatively low laser power involved, does not negatively affect the tissue through heating. It has been used to image several tissues including cartilage, cornea, tendon, ligament and intervertebral disc.[5-7] The same microscope setup can be used to induce two photon fluorescence (TPF), which highlights elastin fibres and calcified tissues.[8] Hence, these two methods provide information on the tissue microstructure, but they also give some hint on their composition. Reliance on endogenous contrast allows for detailed structural data from intact and unstained samples. SHG and TPF imaging are also compatible with Raman micro-spectroscopy, a vibrational spectroscopy technique which can provide highly biochemical-specific information. Raman spectroscopy has been extensively applied to tissues such as bone[9,10] and cartilage.[11,12] The feasibility of using techniques similar to Raman spectroscopy on IVDs has been already demonstrated by a small number of studies.[13-15] However, it is the first time that Raman spectroscopy has been employed to study the vertebral endplate and in conjunction with multiphoton imaging, to reveal chemical and micro-structural information.

This study aimed to explore the structure and chemical composition of the transition across the bony endplate, cartilage endplate and intervertebral disc, below the nucleus and the annulus, regions of very different structure and mechanical properties, in young healthy bovine caudal spines.

Experimental

Bovine sample preparation

Seven functional units (half vertebra, disc, half vertebra) were removed from freshly frozen bovine tails (~1 year of age) obtained from a local abattoir, using an oscillating saw (Makita TM3000C/2). The functional units were cut from the second/third or third/fourth coccygeal vertebrae, depending on the point at which the tails were excised from the spine. Thick slices (about 5 mm) were then cut parallel to the mid-

sagittal plane. The surface of each slice was smoothed using a cryo-microtome (Bright Instruments, OTF 5000) after embedding in frozen Phosphate-buffered solution (PBS). Samples were then transferred to microscope slides and PBS was applied to maintain the hydration of the samples and to avoid shrinkage.

Imaging protocol

Multiphoton imaging and Raman microscopy were performed sequentially on each sample. In order to study in parallel similar regions of the same sample with both techniques, white labels were positioned on the sample to designate areas of interest. The label defined an axis along which a series of images were acquired (ESI Fig. 1†), in order to image a large area, from the trabecular bone of the vertebral body to the intervertebral disc. Morphological features on mineralized tissue were aligned between the white light mode images acquired with Raman microscope and the multiphoton ones and used as markers for the starting point of imaging, whereas different areas (bone, disc) were identified by visual inspection. At the same time, multiphoton imaging was used as a guide to identify the tidemark on each sample and then acquire Raman spectra from individual areas of interest.

Multiphoton imaging

The multiphoton microscopy set up utilised a modified, non-inverted confocal laser scanning microscope (FluoView 300 and Olympus BX51) fitted with a 10x/0.4NA air objective (Olympus UPlanS Apo). An 810 nm mode-locked femtosecond Ti:Sapphire laser (Mira 900-D, Coherent Inc.) was used to excite the SHG and TPF, with a repetition rate of 76 MHz and a pulse width of 100 fs. SHG and TPF were both collected in the *epi*-direction, and the signal separated from the laser fundamental by two filters; a long pass dichromatic filter (670dxr Chroma technologies) and a colour glass filter (CG-BG-39 CVI laser). The SHG and TPF were directed into two separate photomultiplier tubes (PMT) (R3896 Hamamatsu) by a long pass dichromatic filter (Semrock Di02-R405) with additional in the paths for the SHG (Semrock FF01-405/10) and TPF (Semrock FF01-520/70).

In order to image an extended region of interest across the osteochondral transition, a series of images were taken. Images were overlapped by ~50 μm to enable their subsequent reconstruction. During imaging the samples were placed on a saline soaked section of tissue, to maintain hydration whilst also avoiding swelling.

Image reconstruction

Images acquired using the multiphoton microscope contained both the SHG and TPF channels in the form of two single-channel grey images. To view both channels simultaneously, false colouring was required. A composite SHG and TPF image was compiled using the FIJI version of ImageJ (Fiji is just ImageJ (http://fiji.sc/)). Sequential images along the axis from cortical bone toward the disc were stitched using GNU Image

Manipulation Program (GIMP 2.8.18). Raw SHG and TPF images were not processed before image reconstruction.

Image analysis

FIJI allowed the measurement of pixel intensity, which indicate the intensity of the signal detected from TPF and/or SHG. Regions of interest (ROI) were drawn across the tidemark in each of the seven samples imaged, which gave information on the changes in the intensity of the two channels. TPF and SHG intensities will differ based on tissue types, and therefor changes in the TPF/SHG ratio can be indicative of compositional changes.

Raman measurements

For the Raman microscopy measurements, a Renishaw inVia spectrometer was employed (Renishaw plc, New Mills, Wotton-under-Edge, Gloucestershire, GL12 8JR), with a near-infrared diode excitation laser at 785 nm (300 mW). The system was equipped with reflected white light imaging. The laser light was initially focused through the microscope lens (×50 long working objective) onto the sample on a motorised XYZ stage. No polarisers were present in the optical path of the spectrometer.

Individual point spectra were obtained from bone to disc matrix along a line perpendicular to the tidemark in steps of 50 μm in bone and disc and 10 μm in the endplate area. The order of measurements was randomised to reduce the effect of dehydration on the results. For the point measurements recorded from seven samples in total, we used a 600 l mm^{-1} grating that was centred at 1300 cm^{-1} to scan the fingerprint region and at 2700 cm^{-1} for the high wavenumber region. The exposure time was two accumulations of 3 s and the cosmic ray removal option of the software (Wire version 4.1) was applied.

Raman mapping from a single specimen was acquired using the automatic Streamline™ Raman imaging of Renishaw inVia.[16] Raman spectra during mapping were collected with a 10 μm step (x and y direction) in a raster mode and an acquisition time of 30 s per line. External standards (Si, NeAr) were measured as calibration routines prior to each set of measurements.

Raman data analysis

Single Raman spectra were plotted using Origin8 (OriginLab, Northampton, MA, USA). For mapping data analysis, the data were loaded into Matlab R2019a (The Mathworks Inc., Natick, Massachussetts, USA) for pre-processing. The spectra were subjected to baseline correction using asymmetric least squares smoothing[17] ($\lambda = 100$, $i = 10$, $p = 0.001$) and additional cosmic ray removal using a 3×3 window median filter.

Following the pre-processing, spectral ratios were calculated for univariate analysis similarly to previous studies.[10,18] The employment of normalised spectroscopic ratios is essential as the absolute values of spectral bands can be affected by scattering cross-section, sampling volume, orientation, absorption and instrument settings in each measurement.[19]

The following ratios were investigated:

• Mineral to Matrix Ratio (MMR) [959 cm^{-1}/(855 cm^{-1} + 877 cm^{-1} + 922 cm^{-1})]: this characterises the mineral composition of the bone. The primary phosphate vibration (ν_1 symmetric stretching mode) at 959 cm^{-1} is normalised to the amount of collagen matrix (855 cm^{-1} (proline), 877 cm^{-1} (hydroxyproline) and 922 cm^{-1} (proline) of collagen). These collagen peaks are independent of collagen crosslinking modifications.[10,20–22]

• Carbonate to Amide I ratio [1074 cm^{-1}/1665 cm^{-1}]: this measures mineral bone relative to collagen content and indicates bone remodelling.[10,23]

• Carbonate to Phosphate Ratio [1074 cm^{-1}/959 cm^{-1}]: This is a widely used measure of mineral composition in bone.[10]

• Phosphate to Amide I ratio [959 cm^{-1}/1665 cm^{-1}]: This measures mineral content, normalised to the collagen content.[22]

• Proline to Phenylalanine Ratio [(855 cm^{-1} + 877 cm^{-1} + 920 cm^{-1}/1003 cm^{-1})]: this ratio is indicative of collagen content relative to the total protein content of the tissue.

• Chondroitin Sulphate to Amide I ratio [1063 cm^{-1}/1665 cm^{-1}]: this reflects the proportion of sulphated glycosaminoglycans to collagen.[24]

• Proteoglycans to Amide III [1378 cm^{-1}/1245 cm^{-1}]: a marker of relative proteoglycan content. The 1378 cm^{-1} glycosaminoglycan peak does not overlap with mineral peaks and so this measure can be used in both bone and disc.[25]

Results & discussion

Multiphoton imaging of the vertebral endplate

Multiphoton microscopy distinguished the main regions of the endplate: the bony endplate (BEP) and the cartilage endplate (CEP), which is made up of mineralised cartilage (MC) and non-mineralised cartilage (non-MC) as illustrated in Fig. 1. The mineralised tissues (BEP and MC) were most clearly visualised in TPF while the SHG was better at showing the collagenous components of the non-MC and disc (Fig. 2 shows annulus region of the disc). In Fig. 2, the structure of the vertebral bone is clearly visible with characteristic trabecular structure, followed by a high-density region of bone, similar in appearance to cortical bone, indicates the BEP. The BEP and MC show similar intensities of TPF, however, the structure of the MC resembles that of the non-MC rather than bone. The non-MC is distinguishable from the MC due to a higher SHG signal.

The tidemark delineates the transition from the between the mineralised and non-mineralised cartilage and was visualised in both multiphoton imaging modalities (Fig. 2 TPF and SHG, orange arrows). The shift in the SHG to TPF ratio seen in the colour change from blue to green (Fig. 2 Combined), indicates a change in the tissue composition.

Fig. 3 is indicative of the differences noted between the annulus and nucleus. The transition from the non-MC to the
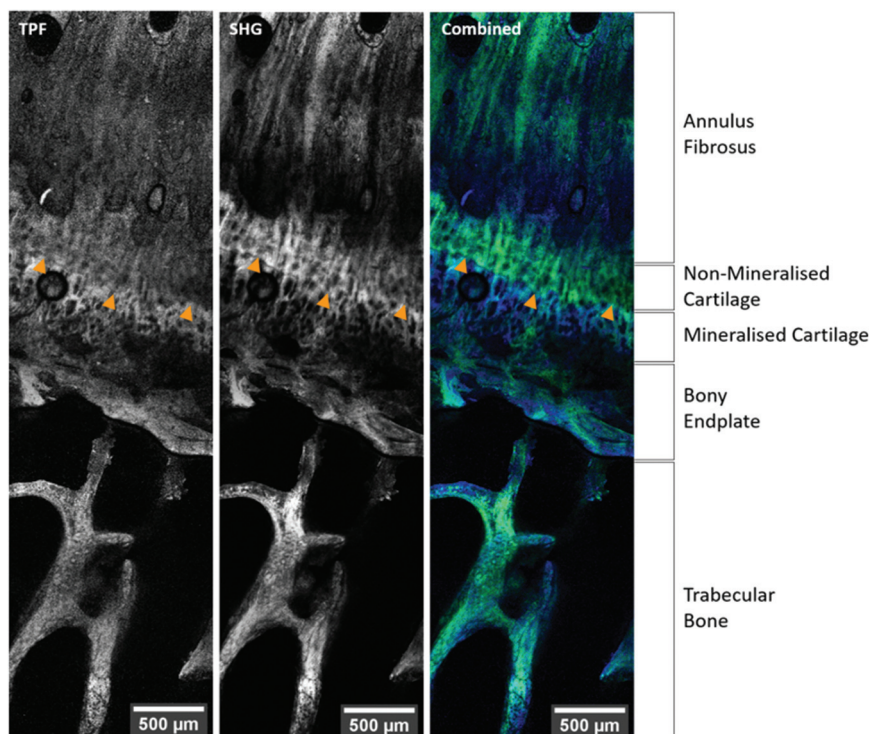
Fig. 2 SHG, TPF and composite multiphoton images of the transition from the trabecular bone to the disc in the bovine tail inner annulus. SHG is false coloured green, and TPF blue. The tidemark is indicated with orange filled arrowheads.
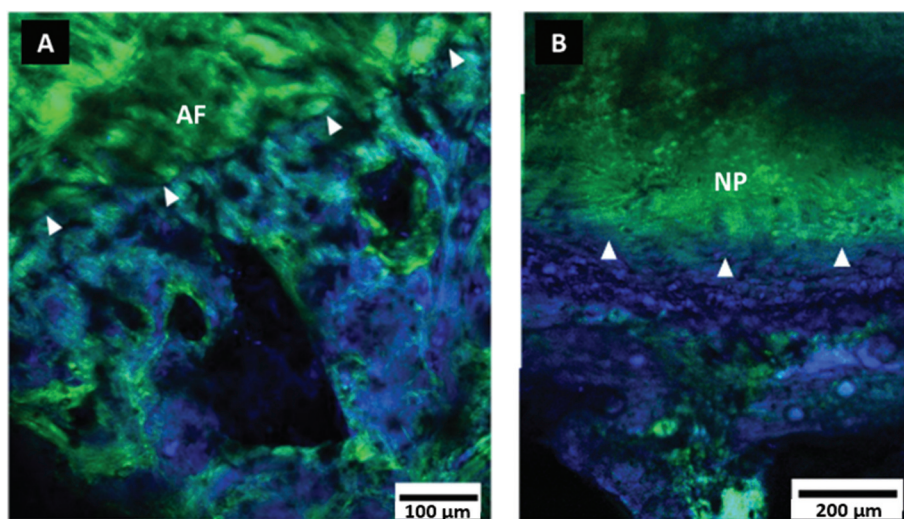

Fig. 3 Multiphoton images of bovine tail endplate. Composite SHG (green) and TPF (blue) images of the tidemark (indicated with white arrow heads) at two regions of the endplate. (A) Outer annulus (B) Nucleus. Images are oriented to transition vertically from disc to bone.

annulus and nucleus, is harder to visualise than the tidemark, as the disc fibres penetrate the non-MC.[26] The nucleus tissues is also harder to visualise due to the absence of directional fibres. The boundary between the non-MC and nucleus is therefore suggested by the loss of the coarse structure visible in the cartilage to a more homogeneous signal in the nucleus. The TM is still visible by the change in TPF/SHG ratio that was previously noted under the annulus in Fig. 3 (indicated with white arrow heads).

Quantification of the observed change in signal intensity across the tidemark is shown in Fig. 4. TPF intensity is higher in the MC, and lower in the non-MC and therefore the tidemark stood out as a step change in intensity. Conversely, the SHG showed an opposite relationship, with a higher intensity
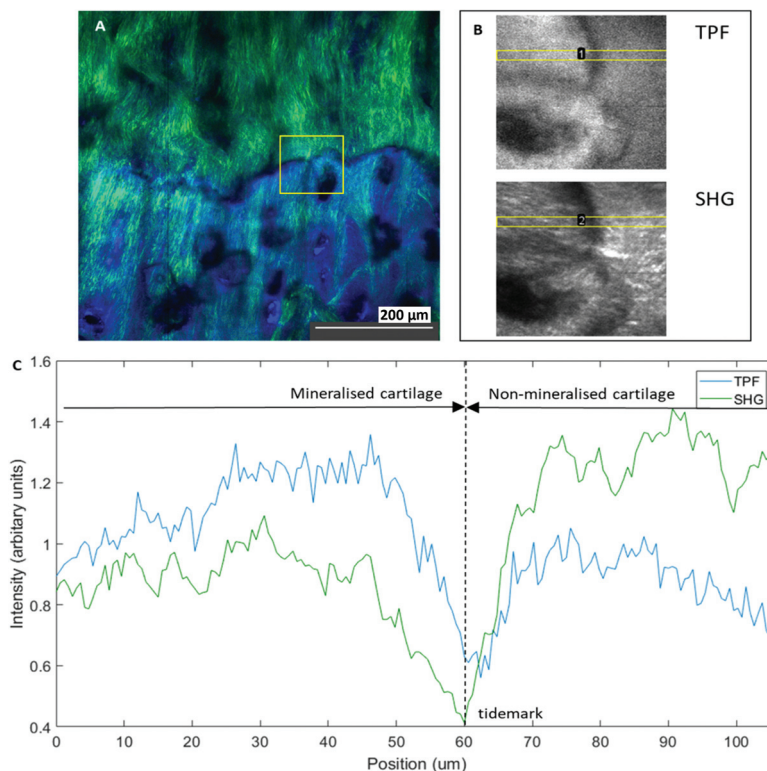
Fig. 4 Decrease in signal intensity at the tidemark. (A) Merged TPF (blue) and SHG (green) multiphoton image of the tidemark. Yellow box indicates ROI used to analyse intensity change across the tidemark (TM). (B) Separated TPF and SHG images taken from (A), rotated 90° right with yellow boxes indicating the ROI used to plot intensity profiles across the TM. (C) Plot profile of the intensities of TPF (blue) and SHG (green) across the tidemark (grey bar).

in the non-MC. Previous work has indicated that MC expresses a higher TPF signal due to the endogenous fluorophores compared to non-MC which carries a stronger SHG signal due to the collagen.[8] Both SHG and TPF showed a steep drop of signal in the 15 μm of disc before the tidemark, however, the SHG signal reaches its lowest intensity 3 μm before the TPF. Both signals show a rapid recovery in the following 5–10 μm, as seen in both the image (B) and the intensity profiles (C) of Fig. 4. This signal gap of ∼3 μm (grey box in Fig. 4) and step change in signal delineates the tidemark (TM) and indicates that there is an abrupt transition between the two types of cartilage present. Fig. 4(A) also suggests continuity of fibre direction between the mineralised and non-mineralised cartilage, seen in the SHG signal indicated by orange asterisk.

Previous studies have employed a similar imaging approach to identify the tidemark of articular cartilage and, in agreement with this study, showed a similar drop in intensity of both SHG and TPF at the tidemark, as well as the change in SHG/TPF ratio, with TPF being higher below the tidemark, and SHG higher above.[8]

The source of a higher intensity of TPF in the MC remains unknown. Suggested explanations for the increased fluorescence below the tidemark include the presence of an additional fluorophore in the MC, which is not present in the non-MC. Previous work has tested pure hydroxyapatite for a TPF signal, however, it was not found to fluoresce.[27] Further, Mansfield *et al.* still reported fluorescence after demineralising samples, suggesting mineralisation is not the cause of the high TPF. Another explanation is that the same fluorophores are present in both the mineralised and non-MC, however, the concentration is greater in the MC. Some previous research has also suggested an association between proteoglycan content and TPF signal.[28] More work is needed to determine the reason for increased fluorescence within the MC as when analysed independently, pure solutions of the proteoglycans hyaluronan, chondroitin sulphate and aggrecan, only the aggrecan produced any TPF and it was not of a significant intensity.[29]

BEP and MC were distinguishable through visible changes in the structure, but almost identical based on TPF and SHG intensities, hence we further employed Raman spectroscopy to identify biochemical changes.

Raman spectroscopic characterisation of the vertebral endplate

Using the multiphoton imaging as a guide ('Imaging protocol' section in Methods and Materials), Raman spectra were

acquired for the individual areas while transitioning from bone to disc: bone, mineralised cartilage (MC), non-mineralised cartilage (non-MC) and disc (Fig. 5(b)).

Raman bands identified in the bone area were consistent with those reported in the literature,[10] including the phosphate (959 cm^{-1}) and carbonate (1074 cm^{-1}) of hydroxyapatite. In the mineralised cartilage adjacent to the bone, the height of the phosphate and carbonate peaks was lower, and they further decreased to zero in the non-mineralised cartilage. Dominant spectral features in the non-mineralised cartilage and the disc area are attributed to proline/hydroxyproline C–C (854, 873 cm^{-1}),[21] proteoglycans (1063, 1378 cm^{-1}),[25,30] amide III (1220–1280 cm^{-1}) and amide I (~1665 cm^{-1}),[31] both assigned primarily to collagen. Due to

the presence of collagen and proteoglycans in the bone and mineralised cartilage, these bands were common between all the areas. A list of the bands observed in the Raman spectra of Fig. 5(b), together with their assignments to vibrational modes are shown in Table 1.

Raman mapping

In order to better understand the endplate transition zone between bone and disc, Raman maps from the area under the nucleus were acquired (Fig. 6). The distribution of matrix and mineral components over the mapping area was evaluated using normalised spectral ratios as described in the Methods and Materials.
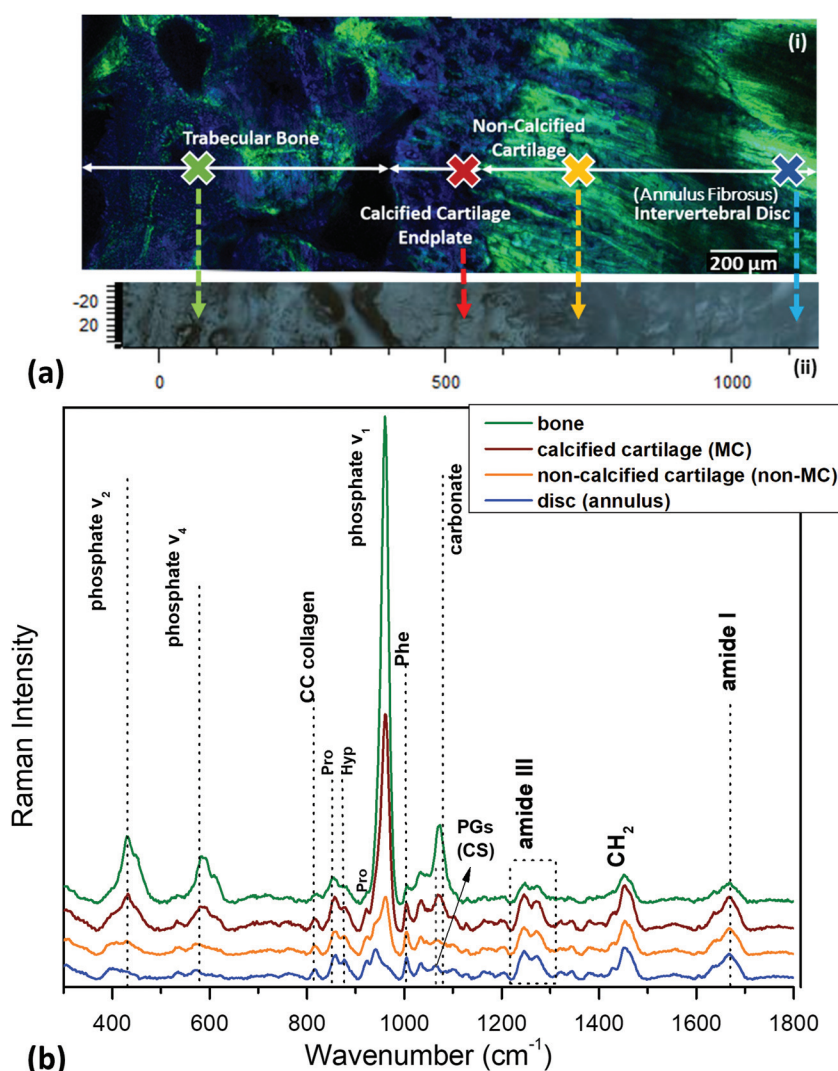

Fig. 5 (a) Acquisition of Raman measurements from a bovine vertebral section (white light montage shown in a(ii)) while using multiphoton imaging (a(i)) as a guide. X marks indicate the location of spectra typical to each area of interest (trabecular bone, calcified cartilage (MC), non-calcified cartilage (non-MC) and disc) under the annulus. (b) Characteristic Raman spectra acquired from the areas of interest designated in Fig. 5(a). The spectral background has been removed, whereas Raman intensities and spectral offset have been adjusted for clarity.

Table 1 Raman shifts (cm^{-1}) and assignments of the bands observed in the areas of interest (bone, mineralised cartilage, non-mineralised cartilage, disc)[10,11,32–36]

Raman shift (cm^{-1})	Assignment
427	ν_2 phosphate stretch
577	ν_4 phosphate stretch
813	C–C of polypeptide collagen backbone
854	(C–C) stretch of proline ring
873	(C–C) stretch of hydroxyproline ring
919	(C–C) stretch of proline ring
938	(C–C) deformation, aggrecan/(C–O–C) stretch, GAG/collagen, ν C–C (protein backbone proline)
959	ν_1 phosphate symmetric stretch
1003	Phenylalanine (C–C) symmetric ring stretch
1033	Phenylalanine (C–C) symmetric ring stretch
1061	SO$_3^-$ symmetric stretch; GAG
1074	ν_1 carbonate stretch
1172	ω CH$_2$ proline
1205	(C-C$_6$H$_5$) stretch; phenylalanine, tryptophan, hydroxyproline, tyrosine
1245	(C–N) amide III
1265	(C–N) stretch alpha-helix; amide III
1318	(CH$_3$, CH$_2$) proline
1340	Glycosaminoglycans, δ C–H (CH$_2$)
1375	Proteoglycans, CH$_3$ symmetric deformation
1426	Glycosaminoglycans, ν_s COO–
1450	(C–H) bend; protein CH$_2$,CH$_3$ scissor
1553	ν C=C aromatic ring (Trp, Tyr)
1667	ν (C=C) and (C=O) stretch alpha-helix; Amide I

Mineral to Matrix ratio (MMR), Carbonate to Amide I and Phosphate to Amide I ratio (Fig. 6b, c, d), all indicated the level of tissue mineralisation, demonstrating high levels across the mineralised part of the endplate compared to the subchondral bone. The Mineral to Matrix Ratio (MMR) corresponds to the relative ratio of the mineral (hydroxyapatite) over the matrix component of the bone (predominantly collagen type I). As the MMR ratio indicates the level of mineralisation in the bone tissue,[37] high values were reasonably observed in the endplate zone but not in the disc area. It should be noted here that the ratio is independent of the collagen type (I or II), as the proline content, and therefore the Raman bands, of the two molecules is similar.[38] Increased Carbonate to Amide I ratio additionally implies decreased bone remodelling of the endplate transition zone.[22,37,39] Organic matrix components, such as proteoglycans (Fig. 6e) and collagen (Fig. 6f), are more prominent in the mineralised part (bone and MC) compared to the non-mineralised part (disc and non-MC).

Although not shown in the main results, amide III ratio (1245/1265 cm^{-1}) (ESI Fig. 2†), which is indicative of the collagen molecular conformational changes,[40] was also analysed over the mapping area. The increased amide III ratio prominent distribution over the disc area implies a highly disordered collagen secondary structure (increased ratio of disordered (random coil: 1245 cm^{-1}) over ordered (a-helix/b-sheet: 1265 cm^{-1}) collagen structure). In the mineralized area, the amide III doublet was found to be less homoge-

neously distributed indicating a more ordered collagen structure in the bone compared to the non-MC and disc area.[35,41]

Spectroscopic comparison of endplate below the nucleus and annulus

To compare the compositional differences of the endplate regions under the nucleus and annulus with Raman spectroscopy, it was necessary to quantify the spectral bands typical to each area of interest (Fig. 7).

Fig. 7 demonstrates higher values of MMR and Carbonate to Amide I ratio under the nucleus compared to the annulus in the bone, MC and non-MC endplate. Both of these ratios are related to the mineral content with Carbonate to Amide I to also indicate bone remodelling.[11,37,39,42] To facilitate visual comparison, the ratios related to the mineralisation are summarised in Fig. 8 (relevant data are available in Table 1 of the ESI†). In the transition from bone to disc, MMR undergoes a steep drop at the MC, continuing through the non-mineralised part. The MMR is marginally higher beneath the nucleus compared to the annulus in the bone, MC and non-MC. A closer look at the individual Raman spectra reveals that, while phosphates and carbonates exist in small amounts in the MC, they are both absent in the non-MC area. However, a weak phosphate contribution seems to be still present in the non-MC area (Fig. 7d). This is in reality a proline νCC skeletal vibration (964 cm^{-1})[33] overlapping with the phosphate band. Interestingly, when transitioning to the disc area this particular proline band disappears resulting in a Phosphate to Amide I ratio close to zero. As it is expected, no Raman bands related to mineral (phosphates or carbonates) are observed in the disc area.

In terms of the carbonate to phosphate ratio (Fig. 7c), similar values are observed under the annulus and nucleus in the bone and MC. As there is a lack of carbonate contribution in the non-MC, the ratio in this area only indicates phosphate levels, which are lower at the MC under the nucleus compared to the annulus. Higher levels of mineralisation under the nucleus are also supported by the Phosphate to Amide I ratio (Fig. 7d), which exhibits higher values in the bone and MC under the nucleus compared to the annulus.

Carbonate to Amide I ratio (Fig. 7b) is also higher in the bone and MC area under the nucleus compared to annulus, indicating a lower degree of remodelling activity at the bone below nucleus.[22] For the non-MC and disc part of Fig. 7b, the Carbonate to Amide I ratio describes in reality the chondroitin sulphate over amide I ratio, as the maximum of the ratio numerator shifts from 1074 cm^{-1} (ν_1 carbonate stretch) to 1063 cm^{-1} (SO$_3^-$ symmetric stretch). This ratio demonstrates the increased chondroitin sulphate content in the non-MC and disc under the nucleus compared to the annulus.

The same trend is observed in Fig. 7f where a second Raman band (1375 cm^{-1}) assigned to proteoglycan content
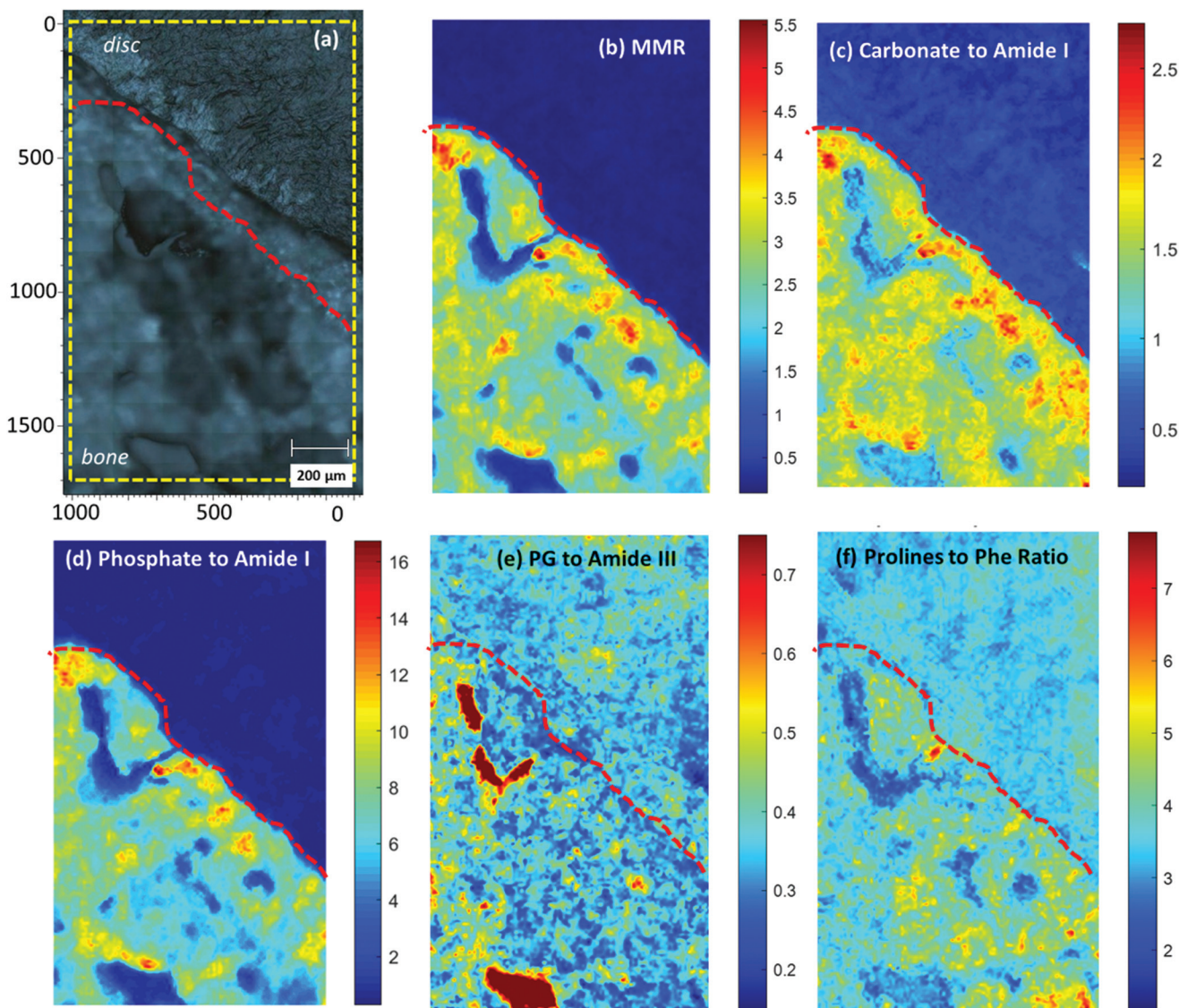
Fig. 6 Raman images (1000 × 1693 um) generated from Raman mapping of an endplate transition zone at the nucleus (white light image of the sample shown in panel (a)), depicting the intensity of different spectroscopic ratios: (b) Mineral to Matrix ratio (959 cm^{-1}/(855 cm^{-1} + 877 cm^{-1} + 922 cm^{-1}), (c) Carbonate to Amide I ratio (1074 cm^{-1}/1665 cm^{-1}), (d) Phosphate to Amide I ratio (959 cm^{-1}/1665 cm^{-1}), (e) Proteoglycans to Amide III ratio (1375 cm^{-1}/1245 cm^{-1}) and (f) Prolines to Phenylalanine ratio (855 cm^{-1} + 877 cm^{-1} + 919 cm^{-1})/1003 cm^{-1}). The yellow subregion marked in panel (a) corresponds to the mapped area with the exact size of panels (b)- (f). The red dotted line in all panels indicates the spectroscopic "tide-mark" between mineralised cartilage and non-mineralised cartilage.

which does not overlap with the carbonate band or any other Raman peak assigned to minerals,[25] is taken into account. Although the proteoglycan to amide III ratio in the bone is very similar under both the nucleus and annulus, the MC under the nucleus exhibits a marginally higher proteoglycan content. Our findings also indicate increased proteoglycan content in nucleus itself compared to annulus (Fig. 7f). This has been spectroscopically confirmed and is in line with previous literature.[43]

Lastly, the normalised to the overall protein content collagen as reflected in the combined prolines to phenylalanine ratio (Fig. 7e), is higher in the bone compared to

disc. FTIR studies on mature articular cartilage have also indicated a collagen content higher in the bone.[24] Our measurements also show evidence of slightly higher levels in the annulus compared to the nucleus, especially towards greater depths of the disc. This is in agreement with previous studies showing decrease of the radial distribution of collagen content in bovine IVDs while moving from outer annulus to inner nucleus.[43] Despite the presence of different collagen types in bone (collagen type I) and disc (collagen type II), the spectral markers employed (proline and hydroxyproline) did not allow us to distinguish between them.[24,25]
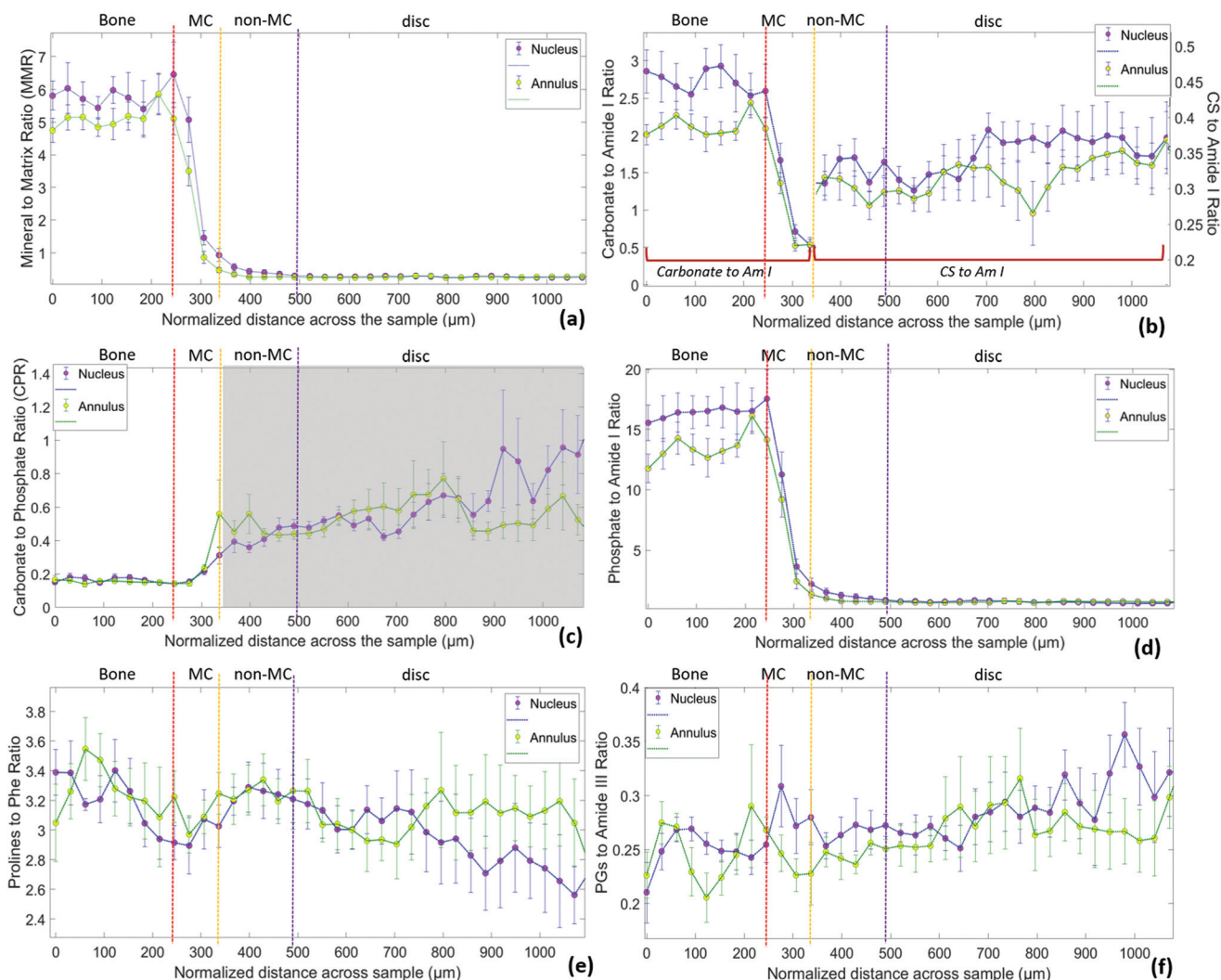
Fig. 7 Raman spectroscopic ratios of 7 bovine samples (average ± SD) as a function of the sample depth in the transition zone from cortical bone to the annulus (green plots) and the nucleus (blue plots). Vertical dashed lines represent the transitions between bone, MC, non-MC and disc. (a) Mineral to Matrix ratio (959 cm^{-1}/(855 cm^{-1} + 877 cm^{-1} + 922 cm^{-1}), (b) Carbonate to Amide I ratio (1074 cm^{-1}/1665 cm^{-1}) for the mineralized part and CS to Amide I ratio (1063 cm^{-1}/1665 cm^{-1}) for the non-mineralized part, (c) Carbonate to Phosphate ratio (1074 cm^{-1}/959 cm^{-1}) which only applies to the mineralized part, (d) Phosphate to Amide I ratio (959 cm^{-1}/1665 cm^{-1}), (e) Prolines to Phenylalanine ratio (855 cm^{-1} + 877 cm^{-1}/1003 cm^{-1}) and (f) Proteoglycans to Amide III ratio (1375 cm^{-1}/1245 cm^{-1}).

It should be also noted that a complicating factor in analysing Raman spectra is that the proline and amide bands are polarisation sensitive,[44] an effect which we have not accounted for in this study.

Raman microscopy revealed a gradient in the composition, between the BEP and MC (Fig. 7). The border between the two regions is marked by an initial sudden drop in the mineral content (phosphates and carbonates) followed by a more gradual decrease to zero in the disc. Other vibrational spectroscopy studies have shown a similar transition between bone and cartilage, tendon or ligament.[19,24,45–47] Our results are also in agreement with previous spectroscopic[19,24,45] and back-scattered electron imaging studies[48] on soft tissue-to-bone transitions. This pattern also

probably reflects a transition of increasing stiffness, from soft to hard tissue.[49,50] It has been suggested that the increase of mineral content enhances the mechanical properties of the disc interface.[50] Although correlation between local stiffness and mineral content has been demonstrated in articular cartilage,[48] further work is needed on the vertebral endplate to relate biochemical properties to the mechanical function of the region.

Conclusions

Our understanding of the vertebral endplate structure has evolved from early descriptions of a uniform 'plate'[51] to that of
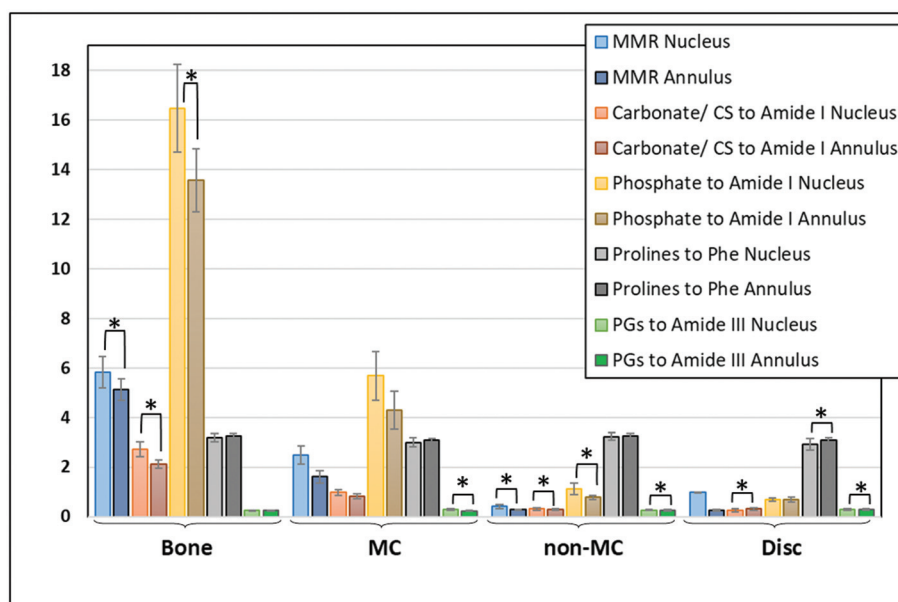
Fig. 8 Mean values of MMR, Carbonate/CS to Amide I, Phosphate to Amide I, Prolines to Phenylalanine and Proteoglycans to Amide III ratios of 7 bovine samples as they were measured in the four different areas of interest (bone, MC, non-MC and disc) across the endplate transition zone under the nucleus and under the annulus. Carbonate to Amide I ratio only applies to the mineralized part (bone, MC), whereas CS to Amide I to the non-mineralized part (non-MC, disc). Asterisks indicate statistical significance of difference ($P < 0.05$) as determined by paired t-test. Relevant data are available in Table 1 of the Supplementary Material.

a multi-layered structure of bone and cartilage[52] and its role in disease is beginning to attract attention. Understanding the structure and physiology of the endplate is key to elucidating this role, specifically regarding disc rupture. The tidemark between the mineralised and non-mineralised cartilage of the endplate has been reported as the failure point in clinical and mechanical investigations suggesting it as a weakness within the functional spinal unit.[53–56] Rodrigues *et al.*, has shown that ovine samples under axial tension failed primarily at the tidemark.[55] Similar findings were found for human specimens, again implicating the boundary between the MC and non-MC as the region of failure, highlighting the importance of understanding this transition zone.[57] However, there is still some evidence of good connectivity between the two regions.[58,59]

Our work contributes to the expanding knowledge of the endplate region through parallel imaging of mineralised and non-mineralised tissues allowing for clear identification of the three endplate regions of the bony endplate, mineralised and non-mineralised cartilage. Here we were not only able to study compositional and structural changes across the endplate zone, but also between the endplate of the annulus and nucleus.

Although the cartilage endplate is a distinct tissue from both the bone and disc as seen by multiphoton microscopy, it acts as a transition zone between the two, bridging between the soft and hard tissue components. The annulus was more easily visualised utilising SHG than the nucleus due to the highly directional fibres, however both regions displayed clear tidemarks between the non-MC and MC. At the same time,

Raman spectroscopy has been able to identify spectral signatures of the chemical profile of the endplate transition zone, demonstrating increased mineralisation levels (MMR, Carbonate to Amide I, Phosphate to Amide I) in the transition endplate zone below nucleus compared to annulus. Little is understood of the mineral content of the endplates, however, some studies have reported on the bone mineral density (BMD), which is suggested to be highest in the peripheral region of the human endplate.[60] Although BMD is not a measure of mineral content, it has been reported that in the spine, bone mineral content is responsible for 86% of variations in BMD.[61] Therefore, it may be that the higher mineral content reported under the nucleus in this study is a characteristic of the bovine tail model, and would not be seen in human endplate. Our findings also indicate that bone remodelling (Carbonate to Amide I ratio) is higher in the bone below the nucleus compared to annulus. High carbonate content is related to low turnover or bone remodelling as carbonate is randomly substituted into the hydroxyapatite crystal for hydroxyl and phosphate groups over time, in that case the age of the bone.[22]

There is no single animal model that is perfect for the human lumbar endplates. This study utilised bovine tail discs and endplates due to their comparable proteoglycan content, absence of notochordal cells at maturation and ease of availability. Due to the endplate's proximity and relationship to both the disc and vertebrae, a model is required that mimics the human in both regards, however, this is currently unavailable.[62,63] The animal model employed in our study, has been previously used extensively in spine research.[64,65]

Limitations of the model relate to the high bone mineral density and fracture stress of bovine vertebral bodies (as previously mentioned).[66]

This study highlights the specificity of the endplate and its role within the disc system, although how these findings relate to the human spine, aging and degeneration still warrants attention. With the understanding of the basic biochemistry and structure at this transitional region to be paramount in future work on preventative and regenerative medicine, our paper contributes to the ongoing necessity for research to 'investigate functional grading across the entire endplate junction'.[57]

Author contributions

Fay Crawford-Manning: Conceptualization, methodology & project administration, formal analysis, data interpretation, writing-original draft, writing- review & editing, approving final version of manuscript; Martha Z. Vardaki: Conceptualization, methodology & project administration, formal analysis, data interpretation, writing-original draft, writing- review & editing, approving final version of manuscript; Ellen Green: Methodology & project administration, approving final version of manuscript; Judith R. Meakin: Data interpretation, writing-review & editing, approving final version of manuscript; Claudio Vergari: Conceptualization, data interpretation, writing- review & editing, approving final version of manuscript; Nick Stone: Data interpretation, writing- review & editing, approving final version of manuscript; C. Peter Winlove: Conceptualization, data interpretation, writing-review & editing, approving final version of manuscript.

Conflicts of interest

The authors declared no potential conflicts of interest with respect to the research, authorship, and/or publication of this article.

Acknowledgements

References

1 J. C. Lotz, A. J. Fields and E. C. Liebenberg, *Global Spine J.*, 2013, **3**, 153–164.

2 R. M. Kanna, R. Shanmuganathan, V. R. Rajagopalan, S. Natesan, R. Muthuraja, K. M. C. Cheung, D. Chan, P. Y. P. Kao, A. Yee and A. P. Shetty, *Asian Spine J.*, 2017, **11**, 594–600.

3 T. S. Jensen, T. Bendix, J. S. Sorensen, C. Manniche, L. Korsholm and P. Kjaer, *BMC Musculoskeletal Disord.*, 2009, **10**, 81.

4 Y. Zhang, B. A. Lenart, J. K. Lee, D. Chen, P. Shi, J. Ren, C. Muehleman, D. Chen and H. S. An, *Spine*, 2014, **39**, E312–E317.

5 C. Vergari, D. Chan, A. Clarke, J. C. Mansfield, J. R. Meakin and P. C. Winlove, *Biomech. Model. Mechanobiol.*, 2017, **16**, 1475–1484.

6 P. Matteini, F. Ratto, F. Rossi, R. Cicchi, C. Stringari, D. Kapsokalyvas, F. S. Pavone and R. Pini, *Opt. Express*, 2009, **17**, 4868–4878.

7 P. Bianchini and A. Diaspro, *J. Biophotonics*, 2008, **1**, 443–450.

8 J. C. Mansfield and C. P. Winlove, *J. Anat.*, 2012, **220**, 405–416.

9 A. Carden and M. D. Morris, *J. Biomed. Opt.*, 2000, **5**, 259–269.

10 M. D. Morris and G. S. Mandair, *Clin. Orthop. Relat. Res.*, 2011, **469**, 2160–2169.

11 K. A. Esmonde-White, F. W. Esmonde-White, M. D. Morris and B. J. Roessler, *Analyst*, 2011, **136**, 1675–1685.

12 C. E. Ramírez, J. M. V. Paredes, E. F. Torales, H. P. L. de Guevara, J. I. D. Saucedo, J. M. R. Castañeda, A. H. Macías, J. M. Montes, J. V. L. Arellano, A. Rodríguez, K. Esmonde-White, M. Z. Vardaki and V. M. Larios, *ISC2 IEEE* 2019, 575–580.

13 K. T. Mader, M. Peeters, S. E. L. Detiger, M. N. Helder, T. H. Smit, C. L. Le Maitre and C. Sammon, *Faraday Discuss.*, 2016, **187**, 393–414.

14 D. Southern, G. Lutz, A. Bracilovic, P. West, M. Spevak, N. P. Camacho and S. Doty, *HSS J.*, 2006, **2**, 49–54.

15 S. R. Sloan Jr., C. Wipplinger, S. Kirnaz, R. Delgado, S. Huang, G. Shvets, R. Härtl and L. J. Bonassar, *JOR Spine*, 2020, e1121.

16 J. Hutchings, C. Kendall, B. Smith, N. Shepherd, H. Barr and N. Stone, *J. Biophotonics*, 2009, **2**, 91–103.

17 P. H. Eilers and H. F. Boelens, *Leiden University Medical Centre Report*, 2005, vol. 1, pp. 5.

18 M. G. Orkoula, M. Z. Vardaki and C. G. Kontoyannis, *Vib. Spectrosc.*, 2012, **63**, 404–408.

19 B. Wopenka, A. Kent, J. D. Pasteris, Y. Yoon and S. Thomopoulos, *Appl. Spectrosc.*, 2008, **62**, 1285–1294.

20 G. S. Mandair, T. A. Bateman and M. D. Morris, *SPIE*, 2009, **7166**, 716607.

21 G. S. Mandair, F. W. Esmonde-White, M. P. Akhter, A. M. Swift, J. Kreider, S. A. Goldstein, R. R. Recker and M. D. Morris, *SPIE*, 2010, **7548**, 754846.

22 H. Isaksson, M. J. Turunen, L. Rieppo, S. Saarakkala, I. S. Tamminen, J. Rieppo, H. Kroger and J. S. Jurvelin, *J. Bone Miner. Res.*, 2010, **25**, 1360–1366.

23 D. H. Kohn, N. D. Sahar, J. M. Wallace, K. Golcuk and M. D. Morris, *Cells Tissues Organs*, 2009, **189**, 33–37.

24 N. T. Khanarian, M. K. Boushell, J. P. Spalazzi, N. Pleshko, A. L. Boskey and H. H. Lu, *J. Bone Miner. Res.*, 2014, **29**, 2643–2652.

25 S. Gamsjaeger, K. Klaushofer and E. P. Paschalis, *J. Raman Spectrosc.*, 2014, **45**, 794–800.

26 R. C. Paietta, E. L. Burger and V. L. Ferguson, *J. Struct. Biol.*, 2013, **184**, 310–320.

27 J. Mansfield, PhD, University of Exeter, 2008.

28 A. T. Yeh, M. J. Hammer-Wilson, D. C. Van Sickle, H. P. Benton, A. Zoumi, B. J. Tromberg and G. M. Peavy, *Osteoarthritis Cartilage*, 2005, **13**, 345–352.

29 J. C. Mansfield, C. P. Winlove, K. Knapp and S. J. Matcher, *SPIE*, 2006, **6089**, 6089O.

30 M. B. Albro, M. S. Bergholt, J. P. St-Pierre, A. V. Guitart, H. M. Zlotnick, E. G. Evita and M. M. Stevens, *NPJ Regener. Med.*, 2018, **3**, 1–11.

31 K. Esmonde-White, *Appl. Spectrosc.*, 2014, **68**, 1203–1218.

32 B. G. Frushour and J. L. Koenig, *Biopolymers*, 1975, **14**, 379–391.

33 J. J. Carcamo, A. E. Aliaga, E. Clavijo, M. Branes and M. M. Campos-Vallette, *J. Raman Spectrosc.*, 2012, **43**, 248–254.

34 N. S. J. Lim, Z. Hamed, C. H. Yeow, C. Chan and Z. J. J. o. b. o. Huang, *J. Biomed. Opt.*, 2011, **16**, 017003.

35 A. Bonifacio, C. Beleites, F. Vittur, E. Marsich, S. Semeraro, S. Paoletti and V. Sergo, *Analyst*, 2010, **135**, 3193–3204.

36 M. Khalid, T. Bora, A. Al Ghaithi, S. Thukral and J. Dutta, *Sci. Rep.*, 2018, **8**, 1–9.

37 B. R. McCreadie, M. D. Morris, T. C. Chen, D. S. Rao, W. F. Finney, E. Widjaja and S. A. Goldstein, *Bone*, 2006, **39**, 1190–1195.

38 M. D. Shoulders and R. T. Raines, *Annu. Rev. Biochem.*, 2009, **78**, 929–958.

39 C. Zhang, P. T. Winnard, S. Dasari, S. L. Kominsky, M. Doucet, S. Jayaraman, V. Raman and I. Barman, *Chem. Sci.*, 2018, **9**, 743–753.

40 K. A. Dehring, A. R. Smukler, B. J. Roessler and M. D. Morris, *Appl. Spectrosc.*, 2006, **60**, 366–372.

41 A. Bonifacio and V. Sergo, *Vib. Spectrosc.*, 2010, **53**, 314–317.

42 H. Isaksson, M. J. Turunen, L. Rieppo, S. Saarakkala, I. S. Tamminen, J. Rieppo, H. Kroger and J. S. Jurvelin, *J. Bone Miner. Res.*, 2010, **25**, 1360–1366.

43 S. E. Bezci, B. Werbner, M. Zhou, K. G. Malollari, G. Dorlhiac, C. Carraro, A. Streets and G. D. O'Connell, *JOR Spine*, 2019, **2**, e1065.

44 L. Van Gulick, C. Saby, H. Morjani and A. Beljebbar, *Sci. Rep.*, 2019, **9**, 1–12.

45 J. P. Spalazzi, A. L. Boskey, N. Pleshko and H. H. Lu, *PLoS One*, 2013, **8**, e74349.

46 M. Orkoula, M. Vardaki, P. Megas, S. Panteliou, C. Kontoyannis and D. Papachristou, Proceedings of 15th Pharmaceutical Panhellenic Conference, 2012.

47 M. Z. Vardaki, D. J. Papachristou, P. Megas, C. G. Kontoyannis and M. G. Orkoula, *Bone*, 2012, **50**, S190–S190.

48 H. S. Gupta, S. Schratter, W. Tesch, P. Roschger, A. Berzlanovich, T. Schoeberl, K. Klaushofer and P. Fratzl, *J. Struct. Biol.*, 2005, **149**, 138–148.

49 V. L. Ferguson, A. J. Bushby and A. Boyde, *J. Anat.*, 2003, **203**, 191–202.

50 C. C. B. Wang, N. O. Chahine, C. T. Hung and G. A. Ateshian, *J. Biomech.*, 2003, **36**, 339–353.

51 H. Gray, R. Warwick; and P. L. WILLIAMS, *Gray's Anatomy*, Longman, 35th edn, 1973.

52 B. Vernon-Roberts, R. J. Moore and R. D. Fraser, *Spine*, 2007, **32**, 2797–2804.

53 M. B. Coventry, R. K. Ghormley and J. W. Kernohan, *JBJS*, 1945, **27**, 105–112.

54 C. Balkovec, M. A. Adams, P. Dolan and S. M. McGill, *Global Spine J.*, 2015, **5**, 360–365.

55 S. A. Rodrigues, A. Thambyah and N. D. Broom, *Spine J.*, 2015, **15**, 405–416.

56 T. P. Green, M. A. Adams and P. Dolan, *Eur. Spine J.*, 1993, **2**, 209–214.

57 B. Berg-Johansen, A. J. Fields, E. C. Liebenberg, A. Li and J. C. Lotz, *J. Orthop. Res.*, 2018, **36**, 192–201.

58 B. Vernon-Roberts and C. Pirie, *Rheumatology*, 1977, **16**, 13–21.

59 S. K. Sinclair, S. Bell, R. T. Epperson and R. D. Bloebaum, *Anat. Rec.*, 2013, **296**, 736–744.

60 M. Muller-Gerbl, S. Weisser and U. Linsenmeier, *Eur. Spine J.*, 2008, **17**, 432–438.

61 H. W. Deng, F. H. Xu, K. M. Davies, R. Heaney and R. R. Recker, *J. Bone Miner. Metab.*, 2002, **20**, 358–366.

62 J. Antoniou, T. Steffen, F. Nelson, N. Winterbottom, A. P. Hollander, R. A. Poole, M. Aebi and M. Alini, *J. Clin. Invest.*, 1996, **98**, 996–1003.

63 C. N. Demers, J. Antoniou and F. Mwale, *Spine*, 2004, **29**, 2793–2799.

64 D. G. Allan, G. G. Russell, M. J. Moreau, V. J. Raso and D. Budney, *J. Orthop. Res.*, 1990, **8**, 154–156.

65 S. Roberts, J. Menage, S. Sivan and J. P. Urban, *BMC Musculoskeletal Disord.*, 2008, **9**, 24.

66 S. R. Sheng, H. Z. Xu, Y. L. Wang, Q. A. Zhu, F. M. Mao, Y. Lin and X. Y. Wang, *PLoS One*, 2016, **11**, e0148610.